Geochemistry, Geophysics, Geosystems

RESEARCH ARTICLE
10.1029/2020GC009253

Key Points:

- Location of permeability barrier at subduction zones is predicted using the numerically calculated thermal structure in the mantle wedge
- Melt flow along the permeability barrier focuses melt produced over a wide region onto a more specific location
- In 28 of 31 locations, the location of the arc is successfully predicted by the apices of the isotherms forming the permeability barrier

Supporting Information:

- Supporting Information S1
- Supporting Information S2

Correspondence to:
G. Ha,
goeunh@terpmail.umd.edu

Citation:
Ha, G., Montési, L. G. J., & Zhu, W. (2020). Melt focusing along permeability barriers at subduction zones and the location of volcanic arcs. *Geochemistry, Geophysics, Geosystems*, *21*, e2020GC009253. https://doi.org/10.1029/2020GC009253

Received 19 JUN 2020
Accepted 12 NOV 2020

Melt Focusing Along Permeability Barriers at Subduction Zones and the Location of Volcanic Arcs

Goeun Ha[1], Laurent G. J. Montési[1], and Wenlu Zhu[1]

[1]Department of Geology, University of Maryland, College Park, MD, USA

Abstract Fluids released from dehydration reactions occurring in subducting slabs trigger partial melting in the mantle wedge. The resulting magma rises through the overlying mantle wedge and lithosphere and forms arc volcanoes at subduction zones. In general, the location of the volcanic arc is narrowly defined even though the melting region in the mantle wedge can be broad. We propose here that a thermally controlled low permeability barrier at the base of lithosphere is able to focus melts to the place where the volcanic arc is actually observed. As the melt ascends, the permeability of the mantle rock decreases as a result of melt crystallization. A low permeability barrier may form in the cooler lithosphere and can trap ascending melt and redirect it laterally according to the slope of the permeability barrier, so that the ascending melt is focused at the apex of the permeability barrier. We model the location and shape of isotherms that approximate the permeability barriers in the mantle wedge based in two-dimensional numerical subduction models that follow the specific geometry of various subduction zones. In 28 of 31 globally distributed test regions, the arc locations estimated from our model show good agreement with the actual arc locations. The modeling results indicate that volcanic arcs can be explained as the surface projection of the apex of the permeability barrier, regardless of the distribution of melt deeper in the mantle wedge.

Plain Language Summary Arc volcanoes are the source of numerous natural hazards as well as many of the gases that form our atmosphere. Despite their importance, it is not yet clear what controls their exact location within the broader geodynamical context of subduction zones. Magma erupted at arc volcanoes may be generated over a broad region in the mantle where water released from the subducting slab can enter. At the surface, though, the arc itself is quite narrow, implying that there is a mechanism collecting and focusing deeply generated magma. We suggest that magmas are guided by a low permeability barrier that forms near the base of the lithosphere where rising magma crystallizes and clogs the passageways through which it is traveling. We show that the location where magma is expected to pool along the permeability barrier matches the actual volcanic arc location at 28 of 31 globally distributed subduction zones. Therefore, it is the temperature structure of the upper plate in subduction zone and the resulting shape of the permeability barrier, not the details of where the slab releases water or the trajectory of fluids rising through the mantle wedge, that controls where volcanic arcs are located.

1. Introduction

Subduction zones often feature a line of volcanoes parallel to the trench forming a volcanic arc, which is probably the surface expression of melt generation and migration processes occurring in the mantle wedge (e.g., Grove et al., 2012; Plank et al., 2013). The addition into the mantle wedge of water released by dehydration of the subducting material triggers partial melting by lowering the mantle solidus temperature (Gill, 1981). The partial melt generated in the mantle wedge then rises through the overlying lithosphere and forms a volcanic arc. Thus, the location of arc volcanoes can provide important constraints on melt generation and migration processes through the mantle.

If the ascending magmas follow a simple vertical trajectory, the arc volcanism should be located directly above the dehydration region (Davies & Stevenson, 1992; Tatsumi, 1986). As it is commonly observed that the volcanic arc lies above the slab with a constant depth of about 110 km where amphibole breakdown occurs (Gill, 1981; Tatsumi, 1986), the main controls of the location of the arc in early studies were a single-phase dehydration accompanied with buoyancy-driven vertical rise of the melts to the crust. Davies

and Stevenson (1992) further developed this model by proposing that the fluids released from the slab by the dehydration of amphibole move laterally into the hotter wedge before generating partial melting. They argued that vertically rising free water rehydrates the overlying mantle and forms amphibole again which is dragged down by the mantle flow and dehydrates again, leading to a relatively small offset between the locus of dehydration and the arc location.

Since then, it has been demonstrated that dehydration is a protracted and sometimes continuous process as various hydrous phases are present in different parts of the slab. Thermo-petrologic modeling indicates that the dehydration reactions in the subducting oceanic crust and mantle can occur at depths greater than 200 km (Hacker et al., 2003; Schmidt & Poli, 1998; van Keken et al., 2011). Recent experimental work demonstrated that amphibole dehydrates at shallower depths than the hydrous melting zone and contributes only a small portion of the water budget in the mantle wedge (Grove et al., 2006, 2009; Schmidt & Poli, 1998). Open system effects can modify where fluids are released from the slab (Tian et al., 2019). Furthermore, the released fluids can migrate to the greater depth due to the downdip flow of the overriding mantle or they can focus toward the wedge corner along a decompaction channel (Cagnioncle et al, 2007; Cerpa et al., 2017; Hebert & Montési, 2013; Wilson et al., 2014). The results from these recent experimental and numerical works imply that the melting region below the arc can be broad due to multiple dehydration steps and fluid migration. Consequently, the region where melt is delivered to the lithosphere is at best only loosely related to where melt is initially produced. This raises important questions: why are most volcanoes clustered along a narrow arc front (England et al., 2004; Syracuse & Abers, 2006), and what are the focusing mechanisms that control the location of arc volcanism?

Several numerical models have found that kinematic variables such as slab dip and convergence velocity influence the size and location of the melting region in the mantle wedge (Cagnioncle et al., 2007; Grove et al., 2009). A fast convergence rate, V_c, increases the vigor of the induced flow and brings hotter mantle further into the wedge corner, widening the melting region. Slab dip, δ, also controls the width of melting region since a shallower slab forms a wider melting region. A compilation of global subduction zones shows that the depth to the surface of the slab below the arc, which is determined by the depth of intraslab seismicity, has a range of 60–200 km and correlates with the descent rate, $V_c \sin \delta$ (England et al., 2004; Syracuse & Abers, 2006). These studies suggested a fundamental correlation between kinematic variables and the position of melting region and arc volcanism. However, consideration of the depth range over which dehydration occurs (van Keken et al., 2011) and diversion of melt migration path as melt rises through the wedge (Wilson et al., 2014) would be expected to blur this correlation.

Many studies proposed mechanisms of melt focusing toward the arc front that potentially affect the position of arc volcanoes. Mantle flow-induced pressure gradients can deviate melt trajectories from being purely vertical (Spiegelman & McKenzie, 1987). Wilson et al. (2014) also suggested a focusing flow driven by compaction pressure gradients, which is produced by variations in porosity in two-phase system. Another proposed focusing mechanism is a sloping high-porosity decompaction channel that is expected to form immediately below an impermeable barrier (Sparks & Parmentier, 1991; Spiegelman, 1993). A crystallization rate large enough to form this impermeable layer can occur around the anhydrous solidus, where a transition from high to low isobaric productivity is expected (Katz et al., 2003). The melts generated within the anhydrous melting region located near the wedge corner may focus toward the nose of the solidus, controlled by circulation in the mantle wedge (England & Katz, 2010). In contrast, Rondenay et al. (2010) suggested that melt is focused along a permeability barrier linked to the thermal structure of the base of the lithosphere. Magma would rise in a predominantly vertical direction if its buoyancy and the permeability of the mantle (Miller et al., 2014, 2016; Zhu & Hirth, 2003) are high enough to overcome the mantle flow. Then, magma would crystallize when it enters the cooler lithosphere. A low permeability barrier is expected to develop as melt connectivity decreases rapidly where crystallization rate is maximum. Variations in the thermal structure of the lithosphere are expected to impart a slope to the decompaction channel. Consequently, melt traveling updip along the decompaction channel also migrates laterally and accumulates at the shallowest reaches of the permeability barrier or potentially where the permeability barrier hits the base of the crust (Rondenay et al., 2010). The volcanic arc is most likely to form immediately above where melt is focused by these deeper melt migration processes, a concept that has been successfully applied to explain the location of volcanic centers at mid-ocean ridges (e.g., Montési et al., 2011).

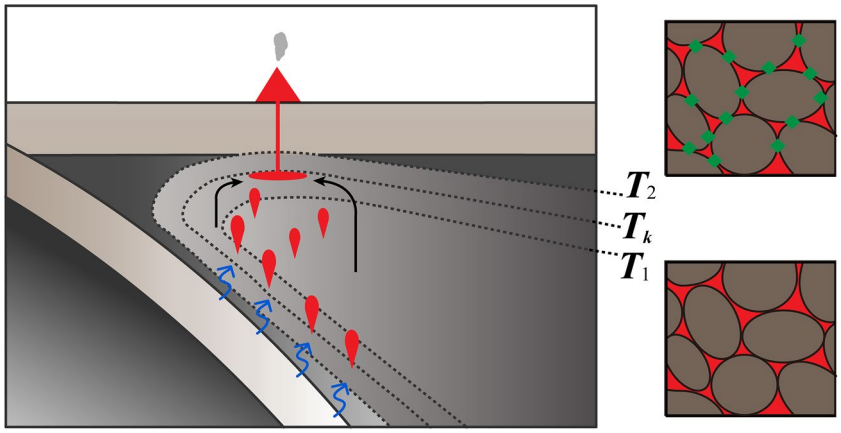

Figure 1. Schematic diagram of permeability barrier formation at mantle wedge. As the slab subducts, dehydration of various subducting hydrous phases releases water over a broad depth range (blue arrows) which triggers partial melting in the mantle wedge (red droplets). The melt rises through the mantle rock at temperature hotter than T_1 by porous flow as shown in the lower right panel, where brown represents solid minerals and red is melt. When the melt enters the cooler lithosphere, it starts to crystallize and clogs the melt pathways in the porous mantle rock. When temperature reaches T_2, all melt pathways are clogged, as shown in the upper right panel, where green diamonds represent crystallized melt. At a temperature T_k between T_1 and T_2, the permeability is low enough to form a barrier to upward melt migration and a decompaction channel forms. The melt can move along the decompaction channel and accumulate at the apex of the barrier. Eventually, the melt accumulated at the apex of the permeability barrier traverses the lithosphere through a combination of thermal erosion, cracking, and diapirism, and forms the volcanic arc.

In this study, we estimate the position of arc by combining the melt focusing concepts from England and Katz (2010) and Rondenay et al. (2010). As the melt rising from the mantle wedge enters the cooler lithosphere, it starts to crystallize and forms a permeability barrier. In the absence of better thermodynamic constraints, we associated the permeability barrier to an isotherm although there is likely to be a pressure dependence on the barrier temperature (Montési & Behn, 2007). The rising melt can then move along and eventually accumulate at the apex of that permeability barrier isotherm (Figure 1). At this point, the crystallizing melt, still releasing heat, thermally erodes the overlying lithosphere and carves into it a vertical pathway to form the arc, as described in England and Katz (2010). Dike and diapir formation can also help the melt traverse the lithosphere (e.g., Keller et al., 2013). Combining these two conceptual models, the location of arc is naturally associated with the apex of the permeability barrier.

We do not have good constraints on how the permeability of mantle rock changes as the hydrous melts crystallize. Instead of using a detailed model, we link conceptually the permeability of mantle rock with high melt crystallization rate. The permeability barrier is most likely to form where the crystallization rate reaches a maximum (e.g., Kelemen & Aharonov, 1998). The temperature-dependent crystallization conditions of melt can be obtained from the previous experimental studies (Grove et al., 2006; Lee et al., 2009). We set the temperature range of barrier formation as 800°C and 1200°C based on the experimentally derived crystallization conditions and assume that the permeability barrier can be formed at any temperature within this range. Schmidt and Poli (1998) suggested that arc volcanoes form above the 1300°C isotherm where the extent of melting is sufficient to allow for the mechanical extraction of parental arc magmas. It is implied in that work that the arc location is close to where temperatures of 1300°C are either the shallowest or the closest to the trench. A cooler temperature is likely relevant in our crystallization-dominated view of the focusing process. We compare the predicted arc location using the permeability barrier model to the observed arc in a global survey of subduction zones. We also examine the systematic relations between the predictions and the subduction parameters.

2. Methods

2.1. Governing Equations and Mantle Rheology

To determine the locations of the permeability barriers constrained by the temperature, first, we calculate the thermal structure in the mantle wedge using two-dimensional (2-D) kinematically driven subduction

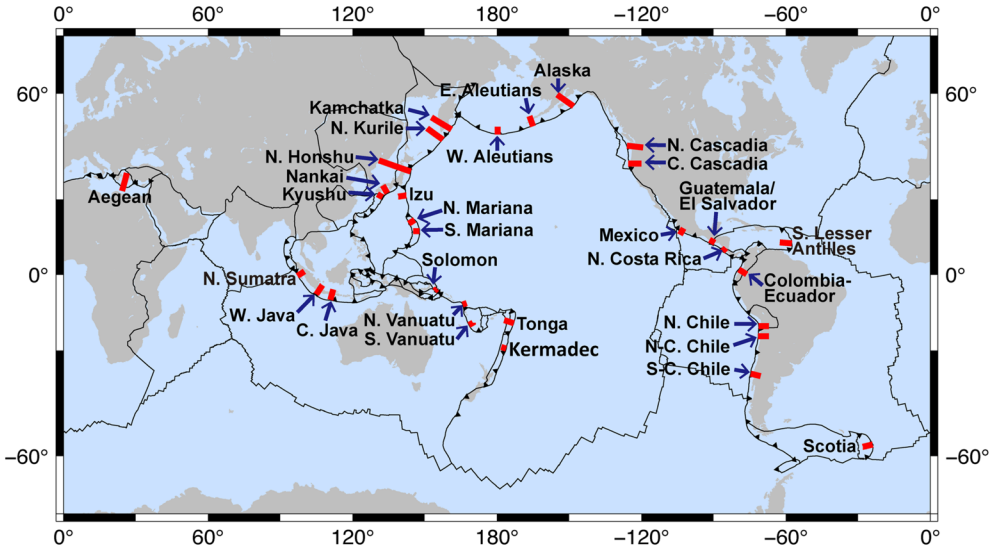

Figure 2. Global map of subduction zones and plate boundaries (Bird, 2003). The barbed black lines represent convergent plate boundaries. The short red lines mark the locations of 31 two-dimensional profiles taken at various subduction zone. Detailed maps of individual subduction zone models are presented in supporting information.

models. We build 31 models each tailored to a specific subduction zone to evaluate globally whether the melt focusing mechanism proposed in this study is generally applicable. As commonly used in previous studies, the model consists of a subducting plate with predefined convergence velocity, a nondeformable overriding plate, and a viscous mantle wedge and sub-slab mantle domain (Currie et al., 2004; Davies & Stevenson, 1992; Furukawa, 1993; Perrin et al., 2018; Syracuse et al., 2010; van Keken et al., 2008; Wada & Wang, 2009). Subjected to the temperature boundary conditions and mantle rheology described below, the mantle temperature and flow fields are calculated by solving the governing equations for the conservation of mass and momentum and the energy equation assuming an incompressible viscous fluid. These governing equations are solved using the default solvers in the commercial finite-element modeling software Comsol Multiphysics®. Solved models are available at Ha et al. (2020).

Many previous subduction models have used either a constant viscosity or diffusion/dislocation creep flow laws to represent the mantle rock rheology (Davies & Stevenson, 1992; Furukawa, 1993). Other numerical and experimental models suggest heterogeneous distribution of the rock rheology in the mantle wedge and upper mantle depending on temperature, pressure, and strain rate (Hirth & Kohlstedt, 2003; van Hunen et al., 2005). In this study, we use a composite viscosity defined as the harmonic mean of the viscosities calculated from diffusion and dislocation creep of olivine in the mantle and subducting plate, while the overriding plate is rigid (Billen & Hirth, 2007; Kneller et al., 2005; van Keken et al., 2008). Detailed information on the viscosity and used parameters is available in Table S2. Although subduction zones are not in a steady state, many numerical studies assume that the model reaches a quasi-steady-state after 20–100 Myr depending on the proximity to the trench or the age of the overriding plate (Kelemen et al., 2003; Syracuse et al., 2010). Here, the model runs until 100 Myr, but we report the thermal structure in the mantle wedge when it reaches a quasi-steady-state at 30 Myr.

2.2. Model Geometry

The locations of 2-D profiles of 31 sites and the associated subduction parameters are shown in Figure 2 and summarized in Table 1. Detailed maps of each subduction zone are presented in Figures S1–S9 and the specific slab shape is available at Ha et al. (2020).

The 2-D slab geometry of each subduction zone is obtained from the compilations of global subduction geometries based on earthquake catalogs Slab 1.0 and Slab2 (Hayes et al., 2012; 2018). Slab depth data are

Table 1
Parameters and Variables for Each Subduction Zone.

Subduction zone	φ/100 (km)	t_{plate}(Myr)	V_c(mm/yr)	δ (°)	H (km)	References for H	t_c (km)	q (mW/m^2)
N. Cascadia[b]	0.7	7	30	20	90	Syracuse et al. (2010)	40	80[c]
C. Cascadia[b]	1.6	11	40	22	90	Wada and Wang (2009), McCrory et al. (2004)	35	80[c]
Nankai[a]	3.9	15	44	36	90	Wada and Wang (2009)	35	69
Mexico[a]	4.2	13	55	36	110	Wada and Wang (2009), Currie et al. (2002)	40	72
Colombia-Ecuador[a]	4.5	16	46	38	110	Wada and Wang (2009)	40	80[c]
S-C. Chile [a]	8.6	25	71	29	80	Wada and Wang (2009), Syracuse and Abers (2006)	40	80[c]
Guatemala/El Salvador[b]	9.6	17	67	57	100 ± 5	England et al. (2004)	45	80[c]
S. Lesser Antilles[b]	10.5	87	18	42	122 ± 5	Syracuse and Abers (2006)	10	80[c]
Kyushu[a]	10.5	27	47	56	105 ± 5	Wada and Wang (2009), England et al. (2004)	30	69
N. Sumatra[a]	11.2	50	40	34	115 ± 5	Wada and Wang (2009), England et al. (2004)	30	120
Alaska[a]	13.3	46	47	38	85 ± 5	Wada and Wang (2009), England et al. (2004)	40	80[c]
N-C. Chile[b]	13.5	43	77	24	110 ± 7	Syracuse and Abers (2006)	40	80[c]
Aegean[b]	15	200	15	30	120	Syracuse et al. (2010)	33	80[c]
N. Costa Rica[a]	17.1	24	80	63	95	Wada and Wang (2009), Syracuse and Abers (2006), Peacock et al. (2005)	30	80[c]
N. Chile[b]	18.2	46	79	30	115 ± 5	Wada and Wang (2009), England et al. (2004)	45	80[c]
N. Mariana[a]	19.6	148	15	62	145 ± 15	Syracuse and Abers (2006)	10	80[c]
W. Aleutians [a]	22.8	55	54	50	95	Wada and Wang (2009), England et al. (2004)	10	75
E. Aleutians[b]	25.3	55	64	46	80 ± 5	England et al. (2004)	35	80[c]
S. Vanuatu[a]	26.2	50	57	67	100 ± 40	Syracuse and Abers (2006)	10	80[c]
Solomon[b]	27.4	31	94	70	154 ± 20	Syracuse and Abers (2006)	10	80[c]
N. Vanuatu[a]	30.8	44	74	71	188 ± 16	Syracuse and Abers (2006)	10	80[c]
Scotia[b]	32.9	60	61	64	95 ± 20	Syracuse and Abers (2006)	10	80[c]
S. Mariana[a]	36.7	140	30	61	115 ± 10	Wada and Wang (2009), England et al. (2004)	10	80[c]
W. Java[b]	39.6	86	61	49	90 ± 7	Syracuse and Abers (2006)	33	80[c]
Kermadec[a]	47.3	100	57	56	95 ± 5	Wada and Wang (2009), England et al. (2004)	10	80[c]
Kamchatka[a]	47.8	100	76	39	95 ± 5	Wada and Wang (2009), England et al. (2004)	30	70
N. Honshu[b]	51.3	129	82	29	104 ± 10	Syracuse and Abers (2006)	40	80[c]
Izu[a]	52.2	140	51	47	130 ± 6	Wada and Wang (2009), England et al. (2004)	10	80[c]
C. Java[b]	54.3	111	68	46	152 ± 11	Syracuse and Abers (2006)	33	80[c]
Tonga[b]	62.7	109	73	52	110 ± 6	England et al. (2004)	10	80[c]
N. Kurile[b]	63.3	106	78	50	80 ± 7	England et al. (2004)	45	80[c]

Note. t_{plate} is the age of the plate at trench, V_c is the convergence velocity of the incoming plate, δ is the slab dip averaged in the direction of maximum dip between 50 and 250 km depth, H is the depth of the slab observed below the arc, t_c is the thickness of the overriding plate, q is the back-arc heat flow, and $\varphi \equiv t_{plate} V_c \sin \delta$ is the thermal parameter defined by Kirby et al. (1996).
[a]Slab geometry is taken from Slab 1.0. [b]Slab geometry is taken from Slab2. [c]Heat flow set to the back-arc global average of Currie and Hyndman (2006).

not available at large depths in some subduction zones. We extend the slab surface to the bottom of the computation domain (600 km) by simply using the same dip as in for the deepest part of where the data are available. In the back-arc side, the overriding crust is defined with a thickness t_c between 10 and 45 km (Syracuse et al., 2010; Wada & Wang, 2009). The entire domain is meshed with triangle and quadrilateral elements with variable resolution. We use the default element types in Comsol Multiphysics®, which are

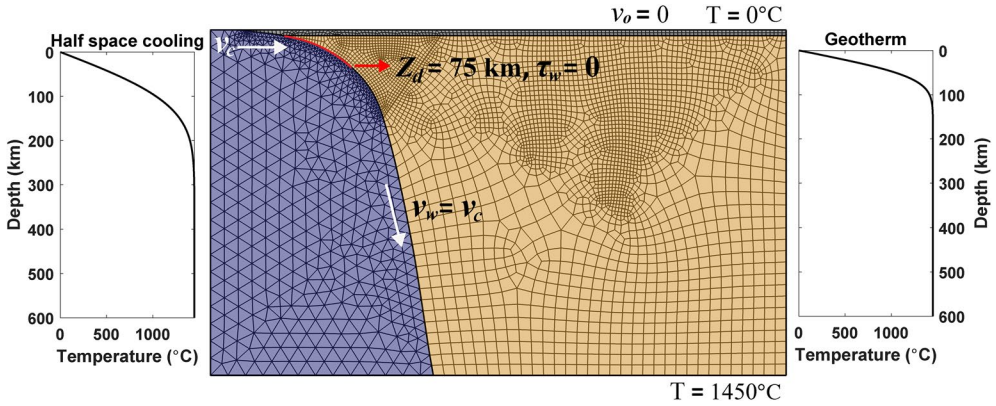

Figure 3. Geometry, meshes, and temperature boundary conditions for the Southern Mariana subduction model. The red line from the wedge corner to Z_d (marked by a red arrow) at 75 km depth represents the boundary where the slab and the overlying mantle are mechanically decoupled; v_c, v_w, and v_o represent with white arrows the velocity of downgoing slab (blue area), mantle wedge (yellow area), and overriding plate (gray area), respectively; and τ_w indicates the shear stress on the mantle wedge side of the subduction interface, which is set to 0 in the decoupled zone (red line). A geotherm based on the age of the incoming plate and the surface heat flow is imposed on the fore-arc side and back-arc side boundary, respectively. A finer mesh is set at the mantle wedge for higher resolution.

P2-P1 elements for fluid flow, and linear elements for heat transport. To use a high mesh resolution where needed without overly increasing computational cost, a maximum element size of 10 km is imposed near the wedge corner (Figure 3). Note that the mesh size in the wedge is often finer than the prescribed maximum size due to geometrical constraints. A few models were repeated with a maximum mesh size of 1 km and showed no significant difference with our results presented here. Figures S1–S9 present the detailed geometry of each model.

2.3. Boundary Conditions

Similarly to the previous subduction zone thermal models (Perrin et al., 2018; Syracuse et al., 2010; van Keken et al., 2008; Wada & Wang, 2009), the mantle wedge flow is induced by the kinematically predefined motion of the subducting slab (Figure 3). Along the slab interface, the convergence velocity of the incoming plate V_c is imposed to induce flow in subducting plate and the underlying mantle. The assigned convergence velocity V_c is the component of the incoming plate motion perpendicular to the trench, which takes into consideration the effect of subduction obliquity (Table 1). The overriding plate velocity is set to zero assuming a nondeformable plate. The mantle wedge is driven by the convergence velocity V_c applied to the subducting interface at a depth greater than a decoupling depth Z_d, whereas a free-slip boundary condition is assigned along the slab interface from the base of the crust to Z_d (Figure 3). Thus the shallow portion of the mantle wedge is decoupled from slab. Decoupling is important to explain fore-arc heat flux, although the origin and exact depth of decoupling remain a matter of debate. Values of 70 km (Currie et al., 2004; Furukawa, 1993), 70–80 km (Wada &Wang, 2009), and 80 km (Syracuse et al., 2010) have been proposed for Z_d. Inspired by these previous studies, the decoupling depth is fixed here to 75 km and applied to all our subduction models. The effect of varying Z_d in one particular model is discussed in Section 4.3. Stress-free open boundary conditions are imposed on each side and at the bottom of the domain (Figure 3).

The surface temperature of the top boundary is set to 0°C and a mantle potential temperature of 1450°C is imposed on the bottom boundary. On the fore-arc side boundary, a geotherm calculated by the GDH1 plate cooling model (Stein & Stein, 1992) is imposed according to the age of the incoming plate at the trench. On the back-arc side boundary, the temperature profile of the overriding crust is set to steady-state conductive profile constrained by heat flow data where available or by the back-arc heat flow global average of 80 mW/m^2 otherwise (Currie & Hyndman, 2006; Wada & Wang, 2009). We include radiogenic heat generation in the crust. Below the overriding crust, temperature increases as an error function with depth, as in the half-space cooling solution of the heat equation, with the heat flow at the top of the mantle the same as that at

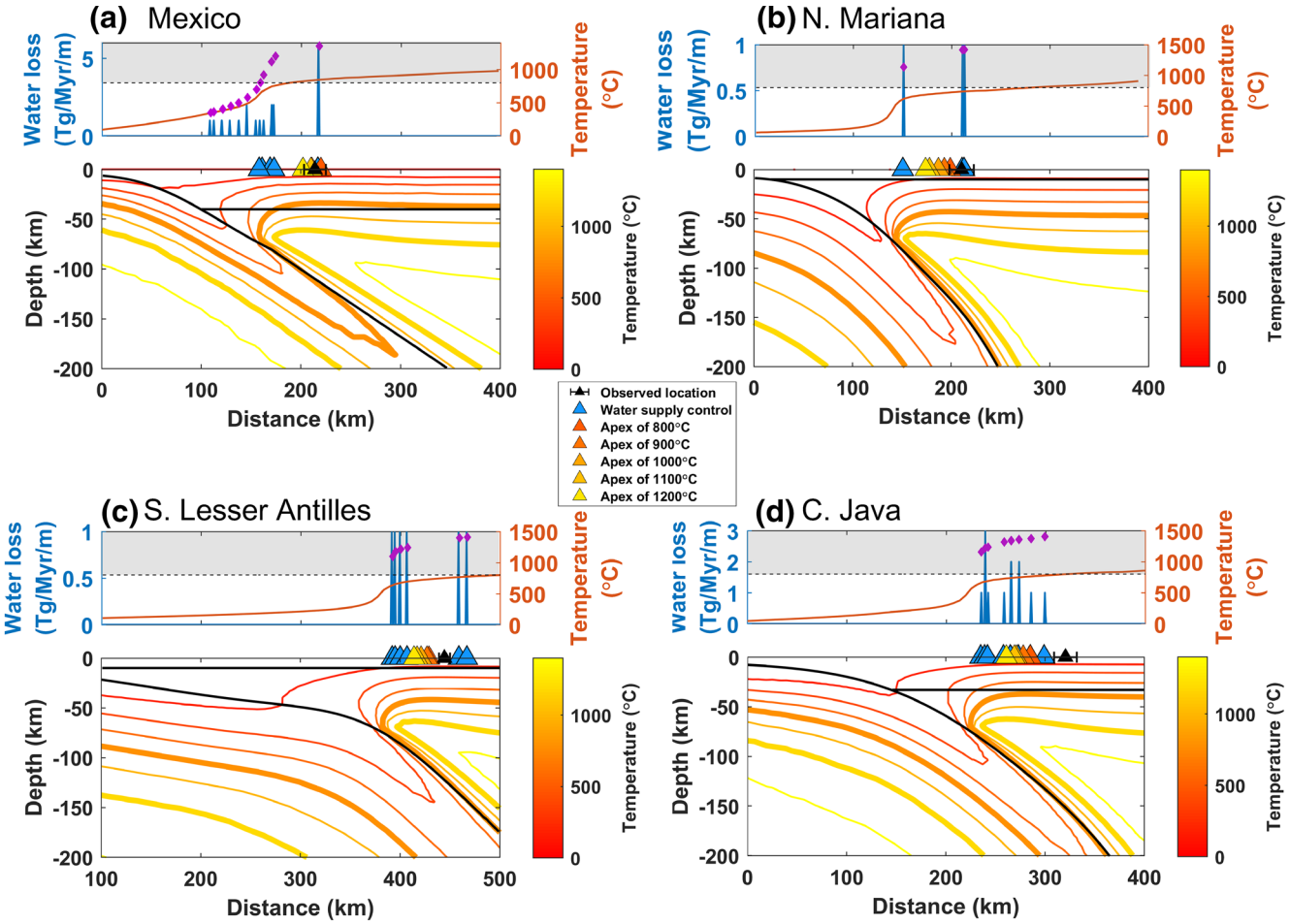

Figure 4. Calculated thermal structure (contours) and the observed and predicted arc location at (a) Mexico, (b) Northern Mariana, (c) Southern Lesser Antilles, and (d) Central Java subduction zone. The black triangle with error bar represents the observed arc location defined by the subarc slab depth *H*. The temperature contours are at 200°C intervals, and the thick orange and yellow contours represent the lower and upper bounds for the formation of permeability barriers, which are 800°C and 1200°C, respectively. The triangles on the surface mark the surface projection of the apex of each isotherm with corresponding color. The graphs above each thermal structure show the slab water loss (blue), the temperature along the slab surface (orange), and the maximum temperature in the mantle wedge above each dehydration site (purple diamonds). The gray shade indicates the area where the temperature is higher than 800°C and melts can form in the mantle wedge. When the maximum temperature in the mantle wedge above the slab dehydration depth is higher than 800°C, the surface projection of slab dehydration depth is shown as a blue triangle in the thermal structure plot.

the base of the crust, and an asymptotic mantle potential temperature of 1450°C. We neglect the thermal effect of shear heating throughout the model, including along the shallowest interface between the slab and overlying mantle. The values of the used parameters are available in Table S2.

3. Results

3.1. Defining Arc Locations

First, we define the arc location in each subduction model based on the previously published subarc slab depth *H* for the associated subduction zone (England et al., 2004; McCrory et al., 2004; Peacock et al., 2005; Syracuse & Abers, 2006; Syracuse et al., 2010; Wada & Wang, 2009). The nominal arc location in each model is defined as the point on the surface where the slab interface reaches the subarc slab depth *H* obtained from the corresponding references (Table 1). We primarily follow the location of the cross section and *H* values presented in Wada and Wang (2009). They mostly obtained the *H* values from England et al. (2004) and Syracuse and Abers (2006). For the subduction zones that are not included in Wada and Wang (2009), we follow the *H* val-

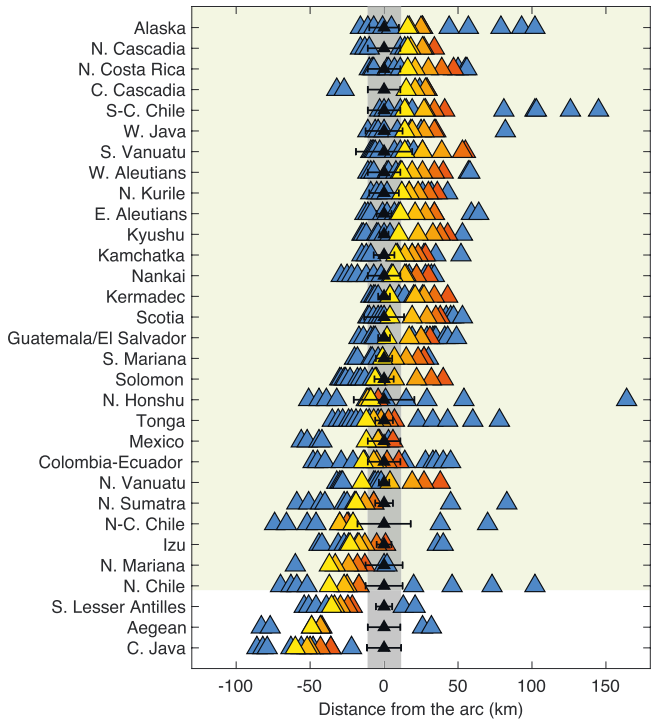

Figure 5. The result of all subduction models. The black triangles at the center with error bar represent the observed arc locations at each subduction zone determined by the averaged subarc slab depth *H*. The gray shaded area represents the averaged width of arc front (±11 km) from 28 subduction zones. The orange to yellow triangles indicate the predicted arc location from the apex of an isotherm between 800°C and 1200°C where a permeability barrier may form. The blue triangles represent the predicted arc location from the slab dehydration depth and wedge temperature. The width of triangles is 10 km, which represents the ascribed arc location prediction uncertainty. The green shaded region highlights subduction zones where the arc location is consistent with focusing along a permeability barrier.

ues obtained from additional references depending on the location of cross section (England et al., 2004; Syracuse & Abers, 2006; Syracuse et al., 2010). In most cases, a range of *H* values is available due to the variability in arc location. In the case where the parameter *H* is determined from a single volcano, we assigned ±11 km horizontal uncertainty obtained by averaging the variability of arc location in the remaining cases. The black triangles with error bar on the surface in Figures 4 and 5 represent the nominal arc location obtained by this method at each subduction zone.

Next, the predicted arc position is determined using the permeability barrier concept. In this case, the melts are generated over a broad region of the mantle wedge and move along the barrier up to its apex. After the melts are focused at the apex, they may rise upward through thermal erosion and form the arc (England & Katz, 2010). Therefore, the surface projection of the apex of the isotherm associated with the permeability barrier serves as the potential arc location.

We consider barrier formation temperatures between 800°C and 1200°C based on experimentally derived crystallization conditions (Grove et al., 2006; Lee et al., 2009). Currently, there are not enough constraints to pick a critical temperature at which the melt pathways are sufficiently blocked to form a permeability barrier. We circumvent this problem by making a range of predictions using five isotherms at 100°C interval between 800°C and 1200°C (Figures 4 and 5). Depending on the shape of isotherm, which is constrained by the temperature field at the mantle wedge and the overriding plate, the predicted arc location based on the permeability barrier varies. By considering the maximum size of the existing volcanoes and magma chambers at the shallow crust, we accept a ±5 km distance between each prediction and the observed arc location.

The region of melt generation by slab dehydration may still be a dominant factor for controlling the location of arc. As previous studies have shown, subducting plates release water over a broad range of depths, which potentially forms a broad melting zone in the mantle wedge. By assuming the simplest buoyancy-driven melts and fluids trajectories, the surface projection of the region where the melts form can be approximated as the position of arc without considering any focusing mechanism. Hence, we report the expected melting region based on the slab water flux data from van Keken et al. (2011) as a comparison to prediction considering melt focusing. To do this, we assume that the released water vertically rises into the mantle wedge and generates melts if the maximum temperature in the mantle wedge is higher than 800°C, which is approximately the mantle solidus underwater-saturated melting condition. Not every dehydration site will lead to melting and a possible arc location in this scenario, as it is possible that the mantle wedge above the dehydration site never experiences temperature above 800°C. Tian et al. (2019) show that considering open-system effects on dehydration reactions can change the pattern of water delivery in the mantle. Although their results are not available for every subduction zone, it is clear that water delivery is more continuous than assumed by van Keken et al. (2011). The dehydration site can change depending on the thermal model used in prediction or slab geometry. We use the dehydration depths from van Keken et al. (2011); however, there will be differences in thermal modeling from this study. Thus, the details of water release are not fully consistent with our model and should not be considered a robust feature of the results predicted here. As the water releases continuously from the slab over a range of depths as previous studies have shown (Tian et al., 2019; van Keken et al., 2011), we can expect that a broad melting region will be formed below the arc regardless of the details of modeling. Once the melts are generated in the mantle wedge, we assume that the buoyancy-driven melts follow a simple vertical trajectory to reach the surface. As will be shown in the next sections, the water release sites are spread over a large horizontal distance, requiring a focusing mechanism to explain the narrow width of volcanic arcs.

3.2. Representative Examples

Figure 4 shows the predicted arc location based on the thermal structure and the nominal arc locations at four representative subduction zones: Mexico, Northern Mariana, Southern Lesser Antilles, and Central Java.

In the Mexico subduction zone (Figure 4a), the majority of dehydration events occur at shallow depth (less than 80 km). However, the wedge temperature is too low to produce melt right above the slab at the shallowest dehydration sites. Deeper dehydration sites, including one water loss peak at ~100 km depth, exceed the lowest bound of the melting temperature. The actual arc at the Mexico subduction zone is located between the predictions made from the slab water loss. However, the arc locations predicted from dehydration melting cover a 59 km wide region, larger than the uncertainty in arc location (±22 km). The isotherm apices are located between 202 and 220 km from the trench, above where the slab is at ~100 km depth and between the shallowest and deepest dehydration-related melt production sites. They are ordered from the hottest (1200°C, yellow) closest to the trench to the coldest (800°C, orange) furthest from the trench. The actual arc location overlaps the apex of the hotter isotherms while the apices of the colder isotherms are further from the trench than the actual arc (Figure 4a).

In the Northern Mariana subduction zone, two major dehydration sites are located at 82 km and 145–148 km depths. The temperature above the slab is high enough to form melts above each dehydration site. As in the case of the Mexico subduction zone, the actual arc is located between the predictions made from the slab water loss, no dehydration takes place immediately below the arc, and the horizontal separation of the two dehydration sites (62 km) exceeds the uncertainty in arc location (±17.5 km). The isotherm apices are similarly ordered over 25 km from hottest nearer the trench to coldest furthest from it. The nominal arc location is further away from the trench than the hottest isotherm apices but overlaps within uncertainty the apices of the cooler isotherms (Figure 4b).

In the Southern Lesser Antilles subduction zone, water dehydrates from the slab from 80 to 90 km depth and again around 140 km depth. The surface projections of these dehydration sites are separated by about 60 km. The actual arc location overlaps the deeper dehydration site within uncertainty. The isotherm apices are located over a 12-km-wide region between the surface projections of the dehydration depth sites and again are ordered from the hottest nearer the trench to the coldest away from it. However, they do not overlap with the observed arc even if location uncertainty is considered (Figure 4c).

In case of the Central Java subduction zone, slab dehydration takes place progressively from 80 to 130 km depth covering a 64-km-wide region at the surface (235–299 km). The isotherm apices are located between the predictions of the dehydration depths over a narrower region from 261 to 286 km from the trench. However, the arc is located 321 ± 12 km from the trench and does not match either set of predicted arc locations (Figure 4d). Once again, the apex of the hottest isotherm considered as a possible permeability barrier is closer to the trench than the cooler ones.

3.3. Result Summary

All predicted and observed arc locations are compiled in Table S1. Figure 5 summarizes the predicted arc location for all 31 subduction models considered in this study. For clarity, the locations are reported in relation to the nominal arc location. The symbols are scaled so that their base spans a characteristic volcano size of 10 km representing ±5 km prediction uncertainty, while the gray shaded region represents the ±11 km average uncertainty in actual arc location. Where available, the actual range of arc location is indicated as a black error bar. In some cases, most notably, Southern Vanuatu, Northern Honshu, and North Central Chile, that error bar is larger than the nominal ±11 km uncertainty.

Arc location predictions based on slab dehydration are shown as blue triangles. In every base but Central Java, the nominal arc location is situated between the end-member sites of melt-inducing fluid release. However, fluid release takes place over a wide depth range, leading to a large range of predicted melt generation, reaching more than 200 km in the extreme case of Northern Honshu. Consideration of open-system effects would further spread water release downward from each dehydration site (Tian et al., 2019). More typically, melting induced by water release is possible over a roughly 80-km-wide span of the surface. While

the actual arc location is typically within that range (Central Java being the one notable exception among all the sites considered), there is not always a water release site immediately below the arc (see the Northern Sumatra, North Central Chile, Izu, and Aegean subduction zones). In other cases, the dehydration site below the arc does not stand out as particularly strong compared to other dehydration sites along the slab.

Arc location predictions made using the apex of isotherms are shown in yellow to orange. In the vast majority of cases, the apex of the hotter isotherm (1200°C, yellow) is also the closest to the trench and the apices of cooler isotherms are located progressively further away from the trench. The arrangement of isotherms reflects the enhanced circulation in the mantle wedge due to temperature-dependent viscosity and the limit of the decoupling zone (Kelemen et al., 2003; Wada et al., 2008). In a few cases, most notably, North Central Chile and Northern Honshu, the order is modified and the various apices are essentially superposed on each other. The apices of the cooler isotherms also overlap in the cases of Tonga, Mexico, and Izu subduction zones. In all other cases, the apices are spread over a region less than 40 km wide. The nominal arc location overlaps within uncertainty with at least one of these apices, typically the hottest one. Only in the three locations discussed in Section 4.2 (Southern Lesser Antilles, Aegean, and Central Java), there is a resolvable difference between arc location and isotherm apex. The subduction zones where arc location is consistent with the apex of one of the possible isotherms for the permeability barrier are highlighted in green in Figure 5. These subduction zones are ordered according to the position of the apex of the 1200°C isotherm. The subduction zones where the arc location is not consistent with the apex of the 1200°C isotherm but that of a cooler one are Northern Vanuatu, Northern Sumatra, Izu, Northern Mariana, and Northern Chile.

4. Discussion

4.1. Melt Focusing at Subduction Zones

Subduction zones generate a significant portion of melt production on the Earth. In particular, they are the source of many of the more evolved volcanic products that are unique to our planet and lead to highly hazardous explosive activity. Melt production is dominated by flux melting that requires introduction of water in the hot mantle wedge. That water is released by dehydration reactions in the downgoing slab. Even though melt generation in this environment is relatively well understood, the processes that control melt migration remain poorly studied. We argue here, based on arc location, that melt focusing along an isotherm associated with the permeability barrier plays an important role in the subduction zone environment, as it does in mid-ocean ridges.

The overall view of subduction zone magmatism that comes from models is that melt can be generated by flux melting over a region that is much wider than the observed arc location (Figure 5, blue triangles). While the arc is indeed located within this broader melt generation zone (with the exception of Central Java), there is rarely a direct match with a specific dehydration reaction, and if there is, there is nothing seemingly exceptional with the specific dehydration reaction that takes place underneath the arc. In some cases, most notably North Central Chile, Izu, Northern Sumatra, and the Aegean subduction zone, the absence of dehydration reactions underneath the arc demonstrates that either melting is formed by a completely different process, or, more likely, that melt is transported laterally over tens of kilometers. Deviations from purely vertical transport are to be expected due to entrainment by mantle flow (Cagnioncle et al., 2007; Hebert & Montési, 2013), pressure gradients generated by corner flow (Spiegelman & McKenzie, 1987), and compaction pressure gradients induced by melt content variations in two-phase system (Wilson et al., 2014). Whether these effects would focus or distribute melt is not generally known but they would affect different melting regions similarly. Regardless, it is unlikely that the region of melt delivery would remain immediately above the various dehydration zones. That, and the narrow width of the volcanic arc compared to the melt generation zone, suggests the presence of melt focusing process unrelated to pressure gradients.

We propose here that melt focusing takes place along an isotherm forming the permeability barrier. As described in the introduction, a permeability barrier forms as a result of temperature-controlled melt crystallization. Rapid crystallization can clog melt pathways in the mantle rock, forming a barrier to upward melt transport and accumulating melt in a decompaction channel underneath the barrier (Sparks & Parmentier, 1991; Spiegelman, 1993). Melt can travel along the channel and pool at the apex of the barrier. In

the context of subduction zones, the permeability barrier can be seen as collecting melt produced over a wide region and focusing it to its thermally controlled apex. The volcanic arc is then expected to form above that melt focusing region (England & Katz, 2010). Its width should be relatively narrow, although predicting it in detail requires a better understanding of magma transport through the lithosphere.

In the context of melt focusing along a permeability barrier, the arc location no longer depends on the details of slab dehydration, melt production, and fluid migration in the mantle wedge. The location of the arc is simply the surface projection of the apex of the isotherm associated with the permeability barrier. This simplified prediction uses only the thermal structure in the mantle wedge and the shape of the permeability barrier currently approximated as an isotherm between 800°C and 1200°C. Using this method, the locations of the actual arc at 28 of the 31 subduction zones considered here are successfully predicted (Figure 5). The three remaining locations are discussed in detail in the next sections. Overall, these simulation results suggest that the permeability barrier model can serve as a viable melt focusing mechanism connecting the dots between a broad melting region and narrow arc front.

In most cases, the hotter and deeper isotherms are more successful at predicting arc location than the cooler ones. This may point to the importance of the anhydrous solidus, that England and Katz (2010) associated with a focusing driven by the transition from high to low isobaric productivity. Although crystallization is not exactly the reverse of melting, and therefore the permeability barrier should not follow a solidus exactly, it is also unlikely to be an isotherm (Hebert & Montési, 2010; Kelemen & Aharonov, 1998). England and Katz (2010) showed that the solidus of approximately anhydrous mantle (actually with 500 ppm water) is crossed underneath most arcs. That solidus is very close to 1200°C. Using the apex of this solidus leads to predicted arc location located only 1–7 km away from the apex of the 1200°C isotherm (Figure S10). Thus, both solidus and isotherm hypotheses are meaningful to describe a focusing mechanism driven by the melt crystallization, especially considering our model does not include latent heat unlike England and Katz (2010). On the other hand, the nose of the region of the mantle hotter than the solidus is systematically closer to the trench than the observed arc location (Figure S11). Only the most extreme cases like the Mexico subduction zone can be explained by the nose of the anhydrous solidus. We note that the difference between the nose and apex of the anhydrous solidus is more pronounced in our models than in England and Katz (2010), probably because of the more complex subduction interface geometry adopted here. Heat transported by magma also can modify the thermal structure of the lithosphere and affect the expected location of the permeability barrier (Rees Jones et al., 2018). Latent heat release is expected to sharpen the apex of the permeability barrier, where magma flux is being focused (England & Katz, 2010). Additionally, detailed petrological modeling is necessary to ascertain the proper location of the permeability barrier matching with the modeled isotherm location.

4.2. Unexplained Regions

The location of the volcanic arc at three locations (Southern Lesser Antilles, Aegean, and Central Java) cannot be explained by focusing along the isotherms according to our models. We discuss here each of these locations and propose reasons for these discrepancies. In all three cases, the isotherm apices are within the region where melting is possible but closer to the trench than the observed volcanic arc.

The subarc slab depth H at the Southern Lesser Antilles subduction zone is 122 ± 5 km, which is deeper than the global average around 105 km. The deepest slab dehydration reaction is at 142 km depth. The arc location predicted by focusing along a permeability barrier is at least 15 km closer to the trench than the observed arc. Reasons for this discrepancy could be a complex slab morphology that is not fully reflected in our model. The Southern Lesser Antilles subduction zone has a relatively short arc with highly curved trench and is located near the thick South American plate (Lynner & Long, 2013; Paczkowski et al., 2014; Figure S2). In this study, we only considered 2-D mantle flow perpendicular to the strike of the trench. However, the along-strike variation of slab dip and curvature can produce pressure-induced trench-parallel mantle flow in the mantle wedge (Jadamec & Billen, 2010; Kneller and van Keken, 2007). In addition, the slab dip changes dramatically at a depth around 50 km from 10° to 45° (Figure 4c), which may indicate that the slab shape is currently changing. In contrast, our model geometry does not change. The thermal structure of the subduction may need tens of millions of years to adjust a change in slab geometry (Rondenay

et al., 2010). The presence of strong trench-parallel mantle flow in the mantle wedge and the delayed adjustment of thermal structure would affect the melt focusing and the simple prediction using the permeability barrier in our steady-state 2-D models may not be valid in this environment.

The Aegean subduction zone has a complex tectonic evolution involving collision between African and Eurasian plate and subsequent extension during African slab rollback (Jolivet et al., 2009; Reilinger et al., 2010). The slab geometry for the Aegean subduction model is taken from a profile crossing the island of Crete. However, that is a point where the trench curvature changes (Figure S8). Subduction obliquity increases from western to central Crete, giving again the possibility of 3-D flow. The subarc slab depth H is defined as 120 km; however, the distance from the trench to the arc is longer compared to the other subduction zones due to the shallow dipping fore-arc slab. Seismic tomography and velocity models suggest that thicker crustal thickness and higher S-wave velocity beneath central Crete compared to the western part of the island (Papazachos & Nolet, 1997; Snopek et al., 2007). Seismic anisotropy study also reveals the presence of trench-normal fast shear wave splitting direction near the trench in the Western Hellenic subduction zone (Olive et al., 2014). That study interprets the trench-normal anisotropy as an indication of rollback-induced mantle flow as the retreating slab drags large volumes of asthenosphere into the upper mantle. Finally, the Aegean sea crust is actively stretching over the location of the Hellenic arc, whereas it is considered rigid in our model. In case of the Aegean subduction zone, the slab rollback and active extension likely affect the thermal structure of the overriding plate and the details of melt focusing. All these phenomena could affect the thermal structure in the Aegean subduction zone.

In the case of the Java subduction zone, localized 3-D mantle flow might change the melt migration path and focusing mechanism. Syracuse and Abers (2006) found that the subarc slab depth H varies by tens of kilometers within arc segments, and the Java subduction zone shows the largest along-strike variation of H over short distances. From Southeastern Sumatra to Western Java, the average subarc slab depth H is 90–100 km, but H increases over 160 km toward Central Java with little slab geometry changes (Syracuse & Abers, 2006). This sudden jump of subarc slab depth H can be an indication of weakened melt focusing, given that the subduction parameters between the Western and Central Java subduction models are similar except for the location of arc. Also, the subarc slab depth at Central Java is unusually large compared to H from the global average unlike that of the Western Java subduction zone, which is around 100 km. To further understand how slab geometry interacts with melt focusing, 3-D subduction models using a more detailed slab geometry are required. However, we show in the following section that changing the decoupling depth makes it possible to explain the observed arc location in Central Java.

There are other limitations, due to many simplifications in our models, that hinder the relation between arc location and focusing mechanism using the permeability barriers. The subarc slab depth H, which we used to determine the actual arc location, relies on slab geometry defined by intraslab seismicity. Depending on the interpretation, the subarc slab depth can vary as previous studies have shown (England et al., 2004; Syracuse & Abers, 2006). These two studies used the EHB catalogs to determine the subarc slab depth, and the H calculated from Syracuse and Abers (2006) is an average of 2 km shallower than those from England et al. (2004). We obtained the subarc slab depth H from several references and each reference used different approaches to define the slab geometry (England et al., 2004; Syracuse & Abers, 2006; Syracuse et al., 2010; Wada & Wang, 2009). We selected the same cross section taken from the referenced papers but adopted the slab geometry from Slab 1.0 and Slab2 (Hayes et al., 2012; 2018). The discrepancy of the slab geometry between these studies and our model could be significant. In the case of Central Java, the slab appears remarkably straight in the cross section of Syracuse and Abers (2006) at a depth below 60 km. The Slab2 model we use does not have this characteristic, which could lead to the nominal arc location being misplaced in our study.

4.3. Subduction Parameters

The observed arc location is generally close to the apex of the permeability barrier, approximated here as an isotherm. The apex of the 1200°C isotherm typically provides the best prediction of the nominal arc location. There are cases, though, where this apex is closer or further away from the trench compared to the volcanic arc. We seek to understand if there are systematic trends in the prediction error from our study,

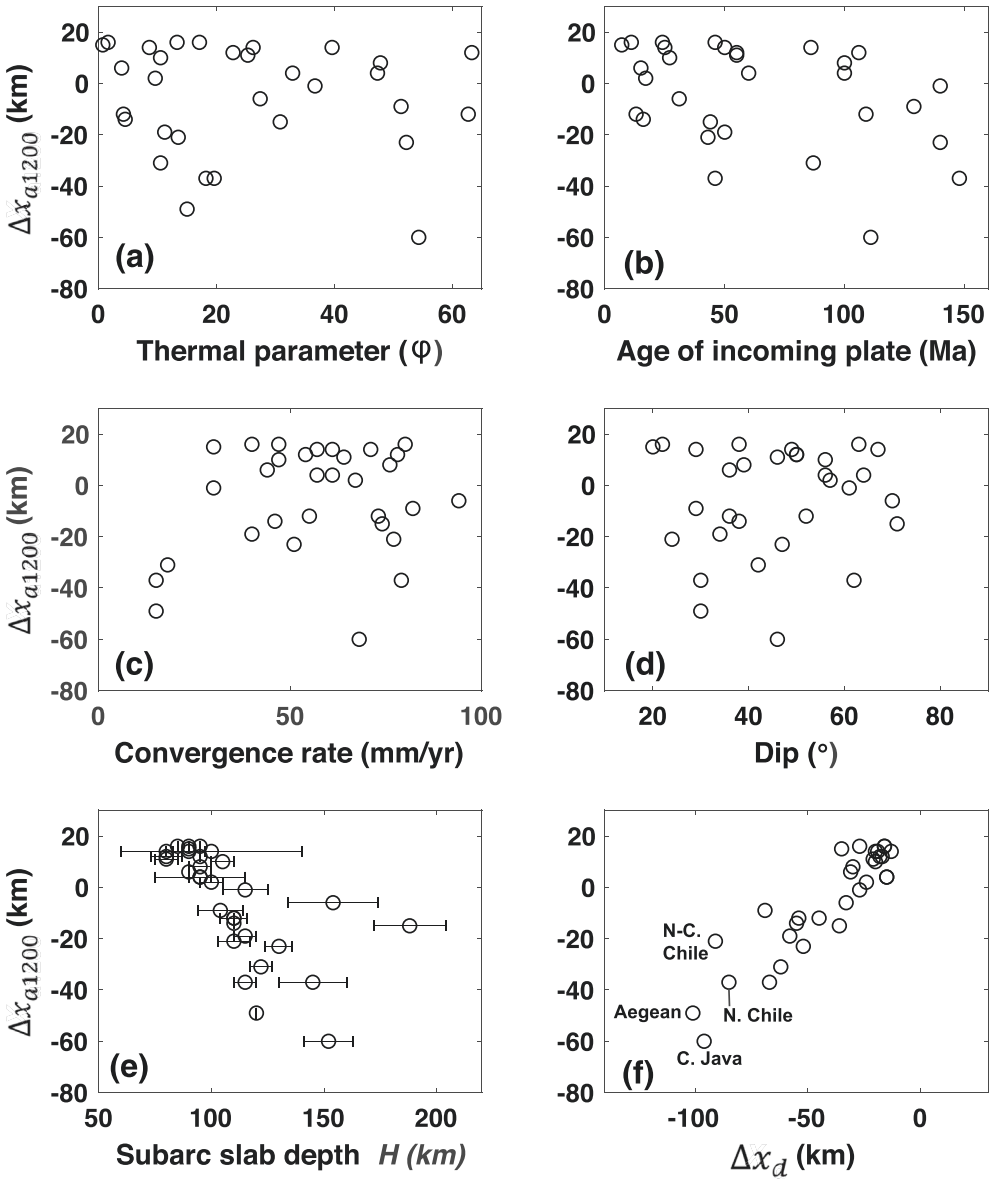

Figure 6. Distance from the observed arc to the surface projection of the apex of 1200°C, Δx_{a1200} versus (a) thermal parameter φ, (b) age of incoming plate, (c) convergence rate, (d) slab dip, (e) subarc slab depth H, and (f) distance from the observed arc to the surface projection of decoupling depth, Δx_d.

which may highlight aspects of the system to focus on in the future. Thus, we examine our modeling results to search for factors that may offset between observed arc location and the 1200°C isotherm apex, Δx_{a1200} (Figure 6).

Most subduction zone parameters show no correlation with the distance between the arc and the apex of the 1200°C isotherm. The prediction from the isotherm apex is primarily dependent on the thermal structure in the mantle wedge, particularly at the base of the lithosphere. By contrast, thermal parameter, age of incoming plate, and convergence rate all express how the slab is heating up in the mantle. Therefore, it may not be surprising that these quantities show no correlation with Δx_{a1200} (Figures 6a–6c). Slab dip influences circulation in the mantle wedge, and therefore heat delivery to the overriding plate and would affect Δx_{a1200} if that circulation were systematically mismodeled. However, no strong correlation is found in our data. The apex of 1200°C isotherm is generally closer to the actual arc location at the larger dip angles (Figure 6d).

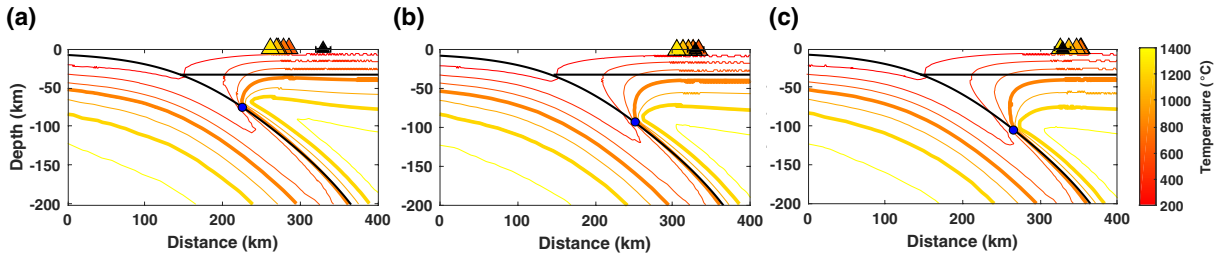

Figure 7. Calculated thermal structure with different decoupling depth of (a) 75 km, (b) 95 km, and (c) 105 km at the Central Java subduction zone. The blue point on the slab represents the end point of the decoupling between the slab and the overlying mantle. As the decoupling depth becomes deeper, the apices of the isotherms move away from the trench, so that the predicted arc locations (orange to yellow) overlap the observed arc location (black triangle with the error bar).

This can be interpreted as a geometrical effect of the slab dip on the shape of the permeability barriers such as the slope and the location of the apex. As the slab dip decreases, the distance from the trench to the arc increases and the trench-ward limit of the isotherm is located closer to the trench from the arc as the previous studies also have observed (Davies & Stevenson, 1992; England et al., 2004; Perrin et al., 2018; Syracuse & Abers, 2006). As a result, the apices of isotherms associated with the permeability barrier also can move toward the trench. This geometrical consideration naturally reduces the possible spread in arc location at the most steeply dipping subduction zones. Conversely, this geometrical effect leads to a larger possible deviation between the predicted arc locations from the permeability barriers and the actual arc locations at shallow dipping subduction zones, as observed (Figure 6d). Several of these subduction zones also have a wavy slab shape which could reflect rollback and a non-steady-state configuration, invalidating central modeling assumptions, as in the Aegean subduction zone.

Figure 6e shows that Δx_{a1200} decreases with increasing subarc slab depth H, which means the accuracy of the prediction decreases as H increases. When H is between 90 and 110 km, the predicted arc locations from the apex of the permeability barriers are the most accurate. This observation indicates that the majority of the predicted arc locations from the permeability barrier is located 90–110 km depth above the slab, which is similar to the global average of subarc slab depth H of 105 km (Syracuse & Abers, 2006). The least accurate prediction corresponds to the Central Java subduction zone, where, as pointed out earlier, there may be inconsistencies in slab geometry definitions. In other cases, 3-D effects, rollback, and stretching may be needed to be included in the models for a more accurate prediction of arc location.

The most significant trend is found between Δx_{a1200} and the distance from the observed arc to the surface projection of decoupling point at 75 km depth, Δx_d (Figure 6f). The closer the arc is to the surface projection of the decoupling depth, the more accurate the prediction from the apex of the isotherm becomes. This trend may indicate that a common decoupling depth to different subduction settings may not be applicable to all subduction zones. The choice of decoupling depth is crucial for our arc location prediction because it produces a cold nose in the subduction zone where isotherms are almost vertical and the closest approach of melting region to the trench is dependent on the decoupling depth (England & Katz, 2010; Perrin et al., 2018; Wada & Wang, 2009). This effect is important for producing a cold fore-arc consistent with low surface heat flow (Syracuse et al., 2010; Wada & Wang, 2009) and seismic attenuation (Currie & Hyndman, 2006; Hyndman & Peacock, 2003). For illustration of this effect, we show in Figure 7 that the predicted arc locations by the isotherm apices move away from the trench as the decoupling depth increases from 95 to 105 km. The example shown is the Central Java subduction zone, where the arc is too far from the trench to be explained by focusing along an isotherm in our regular model (Figure 5). However, isotherm apices overlap with the observed arc location for decoupling depth between 90 and 110 km depth. While the 75 km decoupling depth in our regular models is globally valid (Arcay et al., 2005; Wada & Wang, 2009), values of 90–100 km have previously been considered (Arcay, 2012; Furukawa, 1993). The correlation of Figure 6f can be explained if the decoupling depth at some subduction zones, especially the four highlighted in the figure, is deeper than the nominal value of 75 km. It would probably be possible to find a decoupling depth for each subduction allowing the arc location to be matched by a selected definition of the permeability barrier. However, it would be premature to do so until we have a better handle on the thermodynamics of

permeability barrier formation at subduction zone, fluid trajectory in the wedge, and understanding of both time-dependent effects and along-strike variations in the thermal structure of the mantle wedge.

5. Conclusion

In this study, we show that the temperature-controlled permeability barriers can serve as a melt focusing mechanism and explain the observed arc locations at subduction zones. Modeled arc locations using the focusing mechanism are in good agreement with the actual arc locations in 28 of the 31 subduction zones tested. This focusing mechanism makes it possible to explain the narrow width of volcanic arcs compared to the wider region where slab dehydration and water-fluxed melting can take place. In the case of subduction zones where a strong trench-parallel flow resulting from complex slab geometry is observed, the simplified 2-D trench-perpendicular focusing mechanism cannot explain the observed arc location. Similarly, the overriding plate thermal structure may not be accurately predicted in the case of recent changes in slab geometry or distributed extension in the overriding plate. In the vast majority of subduction zones considered here, though, focusing along a permeability barrier at the base of the overriding plate gives good predictions of the volcanic arc location. In these models, the predicted arc location is controlled solely by the thermal structure of the overriding plate, independently of deeper fluid migration trajectory.

Data Availability Statement

Numerical models for every studied subduction zone, including Comsol Multiphysics® input files and temperatures sampled on a regular grid, are available on Zenodo (Ha et al, 2020).

Acknowledgments
We thank Richard Katz, Ikuko Wada, and an anonymous reviewer for their thoughtful and constructive comments. We also thank Peter van Keken for sharing his prediction of slab dehydration rates. This work is partially supported by the National Science Foundation under grant EAR-1761912 and EAR-1629356.

References

Arcay, D. (2012). Dynamics of interplate domain in subduction zones: Influence of rheological parameters and subducting plate age. *Solid Earth*, *3*(2), 467–488. https://doi.org/10.5194/se-3-467-2012

Arcay, D., Tric, E., & Doin, M. P. (2005). Numerical simulations of subduction zones: Effect of slab dehydration on the mantle wedge dynamics. *Physics of the Earth and Planetary Interiors*, *149*(1–2), 133–153. https://doi.org/10.1016/j.pepi.2004.08.020

Billen, M. I., & Hirth, G. (2007). Rheologic controls on slab dynamics. *Geochemistry, Geophysics, Geosystems*, *8*(8), Q08012. https://doi.org/10.1029/2007GC001597

Bird, P. (2003). An updated digital model of plate boundaries. *Geochemistry, Geophysics, Geosystems*, *4*(3), 1027. https://doi.org/10.1029/2001GC000252

Cagnioncle, A. M., Parmentier, E. M., & Elkins-Tanton, L. T. (2007). Effect of solid flow above a subducting slab on water distribution and melting at convergent plate boundaries. *Journal of Geophysical Research*, *112*, B09402. https://doi.org/10.1029/2007JB004934

Cerpa, N. G., Wada, I., & Wilson, C. R. (2017). Fluid migration in the mantle wedge: Influence of mineral grain size and mantle compaction. *Journal of Geophysical Research: Solid Earth*, *122*, 6247–6268. https://doi.org/10.1002/2017JB014046

Currie, C. A., & Hyndman, R. D. (2006). The thermal structure of subduction zone back arcs. *Journal of Geophysical Research*, *111*, B08404. https://doi.org/10.1029/2005JB004024

Currie, C. A., Hyndman, R. D., Wang, K., & Kostoglodov, V. (2002). Thermal models of the Mexico subduction zone: Implications for the megathrust seismogenic zone. *Journal of Geophysical Research*, *107*(B12), ETG-15. https://doi.org/10.1029/2001JB000886

Currie, C. A., Wang, K., Hyndman, R. D., & He, J. (2004). The thermal effects of steady-state slab-driven mantle flow above a subducting plate: The Cascadia subduction zone and backarc. *Earth and Planetary Science Letters*, *223*(1–2), 35–48. https://doi.org/10.1016/j.epsl.2004.04.020

Davies, J. H., & Stevenson, D. J. (1992). Physical model of source region of subduction zone volcanics. *Journal of Geophysical Research*, *97*(B2), 2037–2070. https://doi.org/10.1029/91JB02571

England, P., Engdahl, R., & Thatcher, W. (2004). Systematic variation in the depths of slabs beneath arc volcanoes. *Geophysical Journal International*, *156*(2), 377–408. https://doi.org/10.1111/j.1365-246X.2003.02132.x

England, P. C., & Katz, R. F. (2010). Melting above the anhydrous solidus controls the location of volcanic arcs. *Nature*, *467*(7316), 700–703. https://doi.org/10.1038/nature09417

Furukawa, Y. (1993). Depth of the decoupling plate interface and thermal structure under arcs. *Journal of Geophysical Research*, *98*(B11), 20005–20013. https://doi.org/10.1029/93JB02020

Gill, J. (1981). *Orogenic andesites and plate tectonics*. Berlin, Germany: Springer-Verlag. https://doi.org/10.1007/978-3-642-68012-0

Grove, T. L., Chatterjee, N., Parman, S. W., & Médard, E. (2006). The influence of H_2O on mantle wedge melting. *Earth and Planetary Science Letters*, *249*(1–2), 74–89. https://doi.org/10.1016/j.epsl.2006.06.043

Grove, T. L., Till, C. B., & Krawczynski, M. J. (2012). The role of H_2O in subduction zone magmatism. *Annual Reviews of Earth and Planetary Sciences*, *40*, 413–439. https://doi.org/10.1146/annurev-earth-042711-105310

Grove, T. L., Till, C. B., Lev, E., Chatterjee, N., & Médard, E. (2009). Kinematic variables and water transport control the formation and location of arc volcanoes. *Nature*, *459*(7247), 694–697. https://doi.org/10.1038/nature08044

Ha, G., Montési, L. G. J., & Zhu, W. (2020). Melt focusing along permeability barriers at subduction zones and the location of volcanic arcs: Numerical models [Data set]. *Zenodo*. https://doi.org/10.5281/zenodo.4256757

Hacker, B. R., Peacock, S. M., Abers, G. A., & Holloway, S. D. (2003). Subduction factory 2. Are intermediate-depth earthquakes in subducting slabs linked to metamorphic dehydration reactions? *Journal of Geophysical Research*, *108*(B1), 2030. https://doi.org/10.1029/2001JB001129

Hayes, G. P., Moore, G. L., Portner, D. E., Hearne, M., Flamme, H., Furtney, M., & Smoczyk, G. M. (2018). Slab2, a comprehensive subduction zone geometry model. *Science*, *362*(6410), 58–61. https://doi.org/10.1126/science.aat4723

Hayes, G. P., Wald, D. J., & Johnson, R. L. (2012). Slab1.0: A three-dimensional model of global subduction zone geometries. *Journal of Geophysical Research*, *117*, B01302. https://doi.org/10.1029/2011JB008524

Hebert, L. B., & Montési, L. G. J. (2010). Generation of permeability barriers during melt extraction at mid-ocean ridges. *Geochemistry, Geophysics, Geosystems*, *11*, Q12008. https://doi.org/10.1002/2010GC003270

Hebert, L. B., & Montési, L. G. J. (2013). Hydration adjacent to a deeply subducting slab: The roles of nominally anhydrous minerals and migrating fluids. *Journal of Geophysical Research: Solid Earth*, *118*, 5753–5770. https://doi.org/10.1002/2013JB010497

Hirth, G., & Kohlstedt, D. (2003). Rheology of the upper mantle and the mantle wedge: A view from the experimentalists. In J. Eiler (Ed.), *Inside the Subduction Factory*. *Geophysical Monograph Series* (Vol. 138, pp. 83–106). Washington, DC: American Geophysical Union. https://doi.org/10.1029/138GM06

Hyndman, R. D., & Peacock, S. M. (2003). Serpentinization of the forearc mantle. *Earth and Planetary Science Letters*, *212*(3–4), 417–432. https://doi.org/10.1016/S0012-821X(03)00263-2

Jadamec, M. A., & Billen, M. I. (2010). Reconciling surface plate motions with rapid three-dimensional mantle flow around a slab edge. *Nature*, *465*(7296), 338–341. https://doi.org/10.1038/nature09053

Jolivet, L., Faccenna, C., & Piromallo, C. (2009). From mantle to crust: Stretching the Mediterranean. *Earth and Planetary Science Letters*, *285*(1–2), 198–209. https://doi.org/10.1016/j.epsl.2009.06.017

Katz, R. F., Spiegelman, M., & Langmuir, C. H. (2003). A new parameterization of hydrous mantle melting. *Geochemistry, Geophysics, Geosystems*, *4*(9), 1073. https://doi.org/10.1029/2002GC000433

Kelemen, P. B., & Aharonov, E. (1998). Periodic formation of magma fractures and generation of layered gabbros in the lower crust beneath oceanic spreading ridges. In W. R. Aharonov (Ed.), *Faulting and magmatism at mid-ocean ridges, Geophysical Monograph Series* (Vol. 106, pp. 267–290). Washington, DC: American Geophysical Union. https://doi.org/10.1029/GM106p0267

Kelemen, P. B., Rilling, J. L., Parmentier, E. M., Mehl, L., & Hacker, B. R. (2003). Thermal structure due to solid-state flow in the mantle wedge beneath arcs. In J. Eiler (Ed.), *Inside the subduction factory, Geophysical Monograph Series* (Vol. 138, pp. 293–311). Washington, DC: American Geophysical Union.

Keller, T., May, D. A., & Kaus, B. J. P. (2013). Numerical modelling of magma dynamics coupled to tectonic deformation of lithosphere and crust. *Geophysical Journal International*, *195*(3), 1406–1442. https://doi.org/10.1093/gji/ggt306

Kirby, S. H., Stein, S., Okal, E. A., & Rubie, D. C. (1996). Metastable mantle phase transformations and deep earthquakes in subducting oceanic lithosphere. *Reviews of Geophysics*, *34*(2), 261–306. https://doi.org/10.1029/96RG01050

Kneller, E. A., & Van Keken, P. E. (2007). Trench-parallel flow and seismic anisotropy in the Mariana and Andean subduction systems. *Nature*, *450*(7173), 1222–1225. https://doi.org/10.1038/nature06429

Kneller, E. A., Van Keken, P. E., Karato, S. I., & Park, J. (2005). B-type olivine fabric in the mantle wedge: Insights from high-resolution non-Newtonian subduction zone models. *Earth and Planetary Science Letters*, *237*(3–4), 781–797. https://doi.org/10.1016/j.epsl.2005.06.049

Lee, C. T. A., Luffi, P., Plank, T., Dalton, H., & Leeman, W. P. (2009). Constraints on the depths and temperatures of basaltic magma generation on Earth and other terrestrial planets using new thermobarometers for mafic magmas. *Earth and Planetary Science Letters*, *279*(1–2), 20–33. https://doi.org/10.1016/j.epsl.2008.12.020

Lynner, C., & Long, M. D. (2013). Sub-slab seismic anisotropy and mantle flow beneath the Caribbean and Scotia subduction zones: Effects of slab morphology and kinematics. *Earth and Planetary Science Letters*, *361*, 367–378. https://doi.org/10.1016/j.epsl.2012.11.007

McCrory, P. A., Blair, J. L., Oppenheimer, D. H., & Walter, S. R. (2004). Depth to the Juan de Fuca slab beneath the Cascadia subduction margin: A 3-D model for sorting earthquakes [CD-ROM]. U.S. Geological Survey Data Series DS-91.

Miller, K. J., Zhu, W., Montési, L. G. J., & Gaetani, G. A. (2014). Experimental quantification of permeability of partially molten mantle rock. *Earth and Planetary Science Letters*, *388*, 273–282. https://doi.org/10.1016/j.epsl.2013.12.003

Miller, K. J., Zhu, W., Montési, L. G. J., Gaetani, G. A., Le Roux, V., & Xiao, X. (2016). Experimental evidence for melt partitioning between olivine and orthopyroxene in partially molten harzburgite. *Journal of Geophysical Research: Solid Earth*, *121*, 5776–5793. https://doi.org/10.1002/2016JB013122

Montési, L. G. J., & Behn, M. D. (2007). Mantle flow and melting underneath oblique and ultraslow mid-ocean ridges. *Geophysical Research Letters*, *34*, (L24307). https://doi.org/10.1029/2007GL031067

Montési, L. G. J., Behn, M. D., Hebert, L. B., Lin, J., & Barry, J. L. (2011). Controls on melt migration and extraction at the ultraslow Southwest Indian Ridge 10°–16°E. *Journal of Geophysical Research*, *116*, B10102. https://doi.org/10.1029/2011JB008259

Olive, J. A., Pearce, F., Rondenay, S., & Behn, M. D. (2014). Pronounced zonation of seismic anisotropy in the Western Hellenic subduction zone and its geodynamic significance. *Earth and Planetary Science Letters*, *391*, 100–109. https://doi.org/10.1016/j.epsl.2014.01.029

Paczkowski, K., Montési, L. G. J., Long, M. D., & Thissen, C. J. (2014). Three-dimensional flow in the subslab mantle. *Geochemistry, Geophysics, Geosystems*, *15*, 3989–4008. https://doi.org/10.1002/2014GC005441

Papazachos, C., & Nolet, G. (1997). P and S deep velocity structure of the Hellenic area obtained by robust nonlinear inversion of travel times. *Journal of Geophysical Research*, *102*(B4), 8349–8367. https://doi.org/10.1029/96JB03730

Peacock, S. M., van Keken, P. E., Holloway, S. D., Hacker, B. R., Abers, G. A., & Fergason, R. L. (2005). Thermal structure of the Costa Rica–Nicaragua subduction zone. *Physics of the Earth and Planetary Interiors*, *149*(1–2), 187–200. https://doi.org/10.1016/j.pepi.2004.08.030

Perrin, A., Goes, S., Prytulak, J., Rondenay, S., & Davies, D. R. (2018). Mantle wedge temperatures and their potential relation to volcanic arc location. *Earth and Planetary Science Letters*, *501*, 67–77. https://doi.org/10.1016/j.epsl.2018.08.011

Plank, T., Kelley, K. A., Zimmer, M. M., Hauri, E. H., & Wallace, P. J. (2013). Why do mafic arc magmas contain ~4 wt% water on average? *Earth and Planetary Science Letters*, *364*, 168–179. https://doi.org/10.1016/j.epsl.2012.11.044

Rees Jones, D. W., Katz, R. F., Tian, M., & Rudge, J. F. (2018). Thermal impact of magmatism in subduction zones. *Earth and Planetary Science Letters*, *481*, 73–79. https://doi.org/10.1016/j.epsl.2017.10.015

Reilinger, R., McClusky, S., Paradissis, D., Ergintav, S., & Vernant, P. (2010). Geodetic constraints on the tectonic evolution of the Aegean region and strain accumulation along the Hellenic subduction zone. *Tectonophysics*, *488*(1–4), 22–30. https://doi.org/10.1016/j.tecto.2009.05.027

Rondenay, S., Montési, L. G. J., & Abers, G. A. (2010). New geophysical insight into the origin of the Denali volcanic gap. *Geophysical Journal International*, *182*(2), 613–630. https://doi.org/10.1111/j.1365-246X.2010.04659.x

Schmidt, M. W., & Poli, S. (1998). Experimentally based water budgets for dehydrating slabs and consequences for arc magma generation. *Earth and Planetary Science Letters*, *163*(1–4), 361–379. https://doi.org/10.1016/S0012-821X(98)00142-3

Snopek, K., Meier, T., Endrun, B., Bohnhoff, M., & Casten, U. (2007). Comparison of gravimetric and seismic constraints on the structure of the Aegean lithosphere in the forearc of the Hellenic subduction zone in the area of Crete. *Journal of Geodynamics*, *44*(3–5), 173–185. https://doi.org/10.1016/j.jog.2007.03.005

Sparks, D. W., & Parmentier, E. M. (1991). Melt extraction from the mantle beneath spreading centers. *Earth and Planetary Science Letters*, *105*(4), 368–377. https://doi.org/10.1016/0012-821X(91)90178-K

Spiegelman, M (1993). Physics of melt extraction: Theory, implications and applications. *Philosophical Transactions of the Royal Society A*, *342*(1663), 23–41. https://doi.org/10.1098/rsta.1993.0002

Spiegelman, M., & McKenzie, D. (1987). Simple 2-D models for melt extraction at mid-ocean ridges and island arcs. *Earth and Planetary Science Letters*, *83*(1–4), 137–152. https://doi.org/10.1016/0012-821X(87)90057-4

Stein, C. A., & Stein, S. (1992). A model for the global variation in oceanic depth and heat flow with lithospheric age. *Nature*, *359*(6391), 123–129. https://doi.org/10.1038/359123a0

Syracuse, E. M., & Abers, G. A. (2006). Global compilation of variations in slab depth beneath arc volcanoes and implications. *Geochemistry, Geophysics, Geosystems*, *7*, (Q05017). https://doi.org/10.1029/2005GC001045

Syracuse, E. M., van Keken, P. E., & Abers, G. A. (2010). The global range of subduction zone thermal models. *Physics of the Earth and Planetary Interiors*, *183*(1–2), 73–90. https://doi.org/10.1016/j.pepi.2010.02.004

Tatsumi, Y. (1986). Formation of the volcanic front in subduction zones. *Geophysical Research Letters*, *13*(8), 717–720. https://doi.org/10.1029/GL013i008p00717

Tian, M., Katz, R. F., Rees Jones, D. W., & May, D. A. (2019). Devolatilization of subducting slabs. Part II: Volatile fluxes and storage. *Geochemistry, Geophysics, Geosystems*, *20*, 6199–6222. https://doi.org/10.1029/2019GC008489

van Hunen, J., Zhong, S., Shapiro, N. M., & Ritzwoller, M. H. (2005). New evidence for dislocation creep from 3-D geodynamic modeling of the Pacific upper mantle structure. *Earth and Planetary Science Letters*, *238*(1–2), 146–155. https://doi.org/10.1016/j.epsl.2005.07.006

van Keken, P. E., Currie, C., King, S. D., Behn, M. D., Cagnioncle, A., He, J., et al. (2008). A community benchmark for subduction zone modeling. *Physics of the Earth and Planetary Interiors*, *171*(1–4), 187–197. https://doi.org/10.1016/j.pepi.2008.04.015

van Keken, P. E., Hacker, B. R., Syracuse, E. M., & Abers, G. A. (2011). Subduction factory: 4. Depth-dependent flux of H2O from subducting slabs worldwide. *Journal of Geophysical Research*, *116*, (B01401). https://doi.org/10.1029/2010JB007922

Wada, I., & Wang, K. (2009). Common depth of slab-mantle decoupling: Reconciling diversity and uniformity of subduction zones. *Geochemistry, Geophysics, Geosystems*, *10*, (Q10009). https://doi.org/10.1029/2009GC002570

Wada, I., Wang, K., He, J., & Hyndman, R. D. (2008). Weakening of the subduction interface and its effects on surface heat flow, slab dehydration, and mantle wedge serpentinization. *Journal of Geophysical Research*, *113*, (B04402). https://doi.org/10.1029/2007JB005190

Wilson, C. R., Spiegelman, M., van Keken, P. E., & Hacker, B. R. (2014). Fluid flow in subduction zones: The role of solid rheology and compaction pressure. *Earth and Planetary Science Letters*, *401*, 261–274. https://doi.org/10.1016/j.epsl.2014.05.052

Zhu, W., & Hirth, G. (2003). A network model for permeability in partially molten rocks. *Earth and Planetary Science Letters*, *212*(3–4), 407–416. https://doi.org/10.1016/S0012-821X(03)00264-4